Whispering-Bloch Elastic Circuits

H.J. Putley[1,*], G.J. Chaplain[1], H. Rakotoarimanga-Andrianjaka[1], B. Maling[1], R.V. Craster[1]

[1] *Department of Mathematics, Imperial College London, London, SW7 2AZ, UK*

Abstract

We investigate structured arrays and rings in elasticity to design elastic platonic circuits that utilise resonant phenomena. Creating ring resonators, and understanding their coupling to input and output arrays, allows for the development of platonic circuits including add-drop filters (ADFs) and coupled resonator elastic arrays (CREAs), and hence we envisage integrated platonic devices. Structured rings of point-masses placed atop a thin-elastic plate lead to highly confined quasi-modes that leak energy; the leakage being quantified by the limiting quality factor $\mathcal{Q}$. The conditions of resonance are deduced using highly accurate numerical simulations based on a Green's function approach to solve the dispersion relation associated with the structured ring resonators. The sharp resonances that emerge are then used to filter and direct wave energy based on input frequency, and this is illustrated through analogy with devices used in optics, e.g. integrated photonic circuits. The potential applications of the elastic devices include elastic delay lines and passive energy harvesters.

Keywords: Platonic, Ring Resonator, Rayleigh-Bloch Mode, Whispering Gallery, Whispering-Bloch Mode, Metamaterial

1. Introduction

Thin-elastic plates support flexural waves and have been much studied particularly in connection with the dynamics of shells [1] and the vibration of periodic engineering structures [2]. More recently, the subject has undergone a renaissance with the analysis of doubly-periodic arrays of supports, [3, 4], revisited from the point of view of phononic crystals [5] with these structured elastic plates being dubbed platonic crystals [6]; the aim being to manipulate and re-direct vibrational wavefields through negative- and ultra-refraction [7, 8], Dirac-like point effects [9, 10] and highly-directive dynamic anisotropy [4, 11] by leveraging Bragg scattering and the interactions due to the periodic structuring.

*Corresponding author.
Email address: h.putley18@imperial.ac.uk (H.J. Putley)

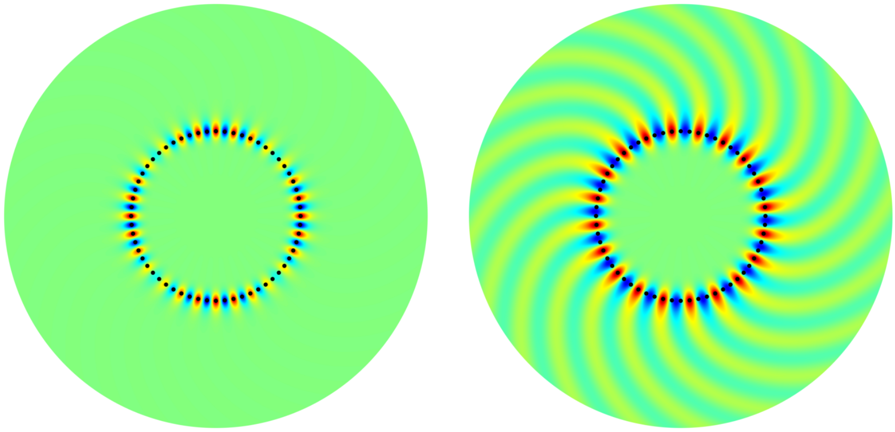

(a) (b)

Figure 1: Structure-located whispering-Bloch modes of a ring resonator consisting of $N = 60$ uniform point-masses (black dots), arranged around a circle, embedded upon a thin-elastic plate obeying Kirchhoff-Love thin plate theory. Normalised wavefield colour scale, red/blue indicating maximum/minimum real displacement.

In the related field of photonics, concerned with structured electromagnetic and optical media, alternative routes for spectral filter design using resonances based on whispering gallery modes have been developed [12]. Micro-Disks, or micro-rings, of one dielectric material embedded within another medium have strong resonances, characterized by high quality-factors at discrete frequencies. Coupling, possibly multiple, resonant micro-disks, or micro-ring resonators created by annular waveguides with index mismatch to the surrounding medium, with adjacent waveguides provides a means to filter, or transfer, wave energy within an integrated optical circuit. Whispering gallery mode resonances are highly sensitive and as such they also find application in bio-sensors [13] and even more widely in nonlinear optics [14]. Devices based upon these resonators are well-established [15, 16] and have been widely developed for telecommunications and optical sensing and many other applications [17]. Despite the success of integrated ring resonators based upon material mismatch there are limitations in the quality-factors that can be achieved due to imperfections and roughness at the surface of the micro-disk and in practical terms, for the frequencies desired, small rings on the scale of microns with high material mismatch are required; these are harder to fabricate and limit the range of materials available which motivates alternative approaches to obtaining resonant structures. One recent approach [18] is to note that structured periodic line arrays can support Rayleigh-Bloch waves that propagate along the array and exponentially decay away from it [19]. Rayleigh-Bloch waves, engendered by some periodic geometry, have arisen in various guises across different areas of wave mechanics, for example in electromagnetism as spoof surface plasmons [20] or those waves sup-

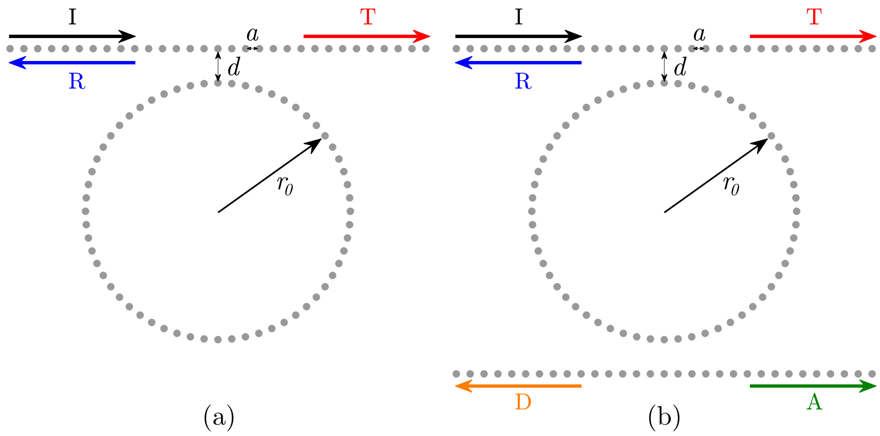

Figure 2: Schematic showing a typical platonic circuit geometry. (a) Structured ring-resonator of radius r_0 separated by a distance d from a neighbouring periodic line array. Incident Rayleigh-Bloch modes along the array couple into the ring and this results in a measured fall in through-transmission T. (b) Add-drop filter with the structured ring resonator coupling to two line arrays, with transmission coefficients D and A measuring mode propagation along the drop- and add-ports respectively.

ported by Yagi-Uda antennas [21, 22]. When the array is curved to create a circular structured array then a strongly localised resonance exists, with high quality-factor, that shares some features of whispering gallery modes but the modes are now created by periodic structuring as in Bloch waves and as such are termed whispering-Bloch (WB) modes [18], as shown in Fig. 1.

The electromagnetic and optical fields, which govern the photonic devices, satisfy Maxwell's equations that reduce, if polarised, to Helmholtz equations, whereas flexural waves in elastic plates, for Kirchhoff-Love theory, obey a fourth-order plate equation that is not simply a Helmholtz equation; none the less Rayleigh-Bloch waves can exist under some circumstances and propagate along mass-loaded periodic line arrays on elastic plates [23]. Given the interest in filtering and manipulation of flexural wavefields we explore the potential of ring resonators created by periodic structuration to create flexural wave filters. The article is structured such that in Sect. 2 we set out Kirchhoff-Love thin plate theory and scattering by N arbitrarily positioned inclusions. In Sect. 3 we analyze the infinite line array of equally-spaced point-masses that supports Rayleigh-Bloch modes and reproduce the dispersion bands of [23]. Section 4 describes the formulation of whispering-Bloch modes of complex wavenumber determined via the winding number method of [24], and the extraction of the limiting quality-factor $\mathcal{Q}$. Combining these resonant devices in Sect. 5 we devise platonic circuits of type drawn schematically in Fig. 2 and demonstrate a high level of control in the filtering and directing of flexural waves, coining the phrase CREAs for coupled resonator elastic arrays. We draw conclusions in Sect. 6 and discuss several practical applications of these platonic circuits.

2. Kirchhoff-Love Theory of Thin Plates

Classical Kirchhoff-Love (KL) theory [25] models the out-of-plane vibrations of thin-elastic plates, and makes the kinematic assumptions of preservation of both plate thickness and straight lines normal to the mid-surface plane after deformation. KL theory remains valid at vibrational wavelengths greater than 20 times the plate thickness [26], a consideration we avoid in the numerics herein by introducing non-dimensional variables parameterising the plate and embedded inclusions, consistent with [23]. The displacement of a thin-elastic plate perpendicular to the x-y plane under excitation by an incident wave-field, assuming a time-harmonic variation of radian frequency ω, is written as $U(\mathbf{r},t) = \mathrm{Re}\{u(\mathbf{r})e^{-i\omega t}\}$ where $u(\mathbf{r})$ is the out-of-plane displacement at the in-plane position $\mathbf{r} = (x, y)$. The equation of motion governing the propagation of flexural waves in an isotropic, homogeneous plate, in the absence of external forces, is

$$D(\nabla^4 - k^4)u(\mathbf{r}) = 0 \tag{1}$$

where ∇^2 is the two-dimensional Laplacian operator and $k^4 = m_p\omega^2/D$ where k is the wavenumber of free waves in the plate, $D = Eh^3/12(1-\nu_p^2)$ the bending modulus, E the Young's modulus, h the plate thickness, ν_p the Poisson ratio and m_p the mass per unit area of the plate. Eq. (1) is modified by the introduction of time-harmonic point-forcings, for which we introduce the infinite plate Green's function $g(\mathbf{r},\mathbf{r}';k)$, which itself is expressed in terms of Hankel functions

$$g(\mathbf{r},\mathbf{r}';k) = \frac{i}{8k^2}\left\{H_0(k\rho) - H_0(ik\rho)\right\} \tag{2}$$

where $\rho = |\mathbf{r}-\mathbf{r}'|$ and H_0 is the Hankel function of the first kind and order zero. The Green's function (2) represents the field at point $\mathbf{r}$ due to a point-forcing at $\mathbf{r}'$ upon the platonic surface, and satisfies the modified equation of motion

$$(\nabla^4 - k^4)g(\mathbf{r},\mathbf{r}';k) = \delta(\mathbf{r}-\mathbf{r}'). \tag{3}$$

Notably this Green's function is bounded as $\mathbf{r} \to \mathbf{r}'$, which makes it ideal as a building block to solve for the scattering of flexural vibrations by infinite arrays, or finite numbers, of point-forcings [23]. The non-singular nature of (2) allows for the determination of the flexural wavefield globally, with each point-forcing corresponding to a Green's function (2) in summation. Following the derivation in [23], for an array of N point-forcings at arbitrary positions $\mathbf{r}_n$, where $n = 0 \dots N-1$ the displacement $u(\mathbf{r})$ obeys

$$D(\nabla^4 - k^4)u(\mathbf{r}) = D\sum_{n=0}^{N-1} A_n\delta(\mathbf{r}-\mathbf{r}_n) \tag{4}$$

where DA_n is the forcing at $\mathbf{r}_n$; if this is assumed proportional to the displacement at the point then an impedance $\mu_n D$ characterises this and $DA_n = \mu_n D u(\mathbf{r}_n)$. Evans and Porter [23] introduce the impedance parameter

$$\mu_n = 4k^4a^2\tilde{\mu}_n + i4k^2\tilde{\nu}_n, \tag{5}$$

which is related to the mass M at the point, and a characteristic length-scale a via the non-dimensional parameters

$$\tilde{\mu}_n = \frac{1}{4m_p a^2} M_n, \qquad \tilde{\nu}_n = -\frac{1}{\sqrt{16Dm_p}} \nu_n, \tag{6}$$

where we introduce point-wise damping ν_n at each loading point; these points are described as mass-loaded with a damping restoring force. The Green's function (2) is placed in the summation over point position such that, in the presence of an incident field $u_i(\mathbf{r})$, the total wavefield satisfying (4) is

$$u(\mathbf{r}) = u_i(\mathbf{r}) + \sum_{n=0}^{N-1} A_n g(\mathbf{r}, \mathbf{r}_n; k). \tag{7}$$

A system of N equations for the amplitudes of the Green's functions follows:

$$A_m = \mu_m u_i(\mathbf{r}_m) + \mu_m \sum_{n=0}^{N-1} A_n g(\mathbf{r}_m, \mathbf{r}_n; k) \tag{8}$$

for $m = 0 \ldots N-1$.

Noting that $g(\mathbf{r}_m, \mathbf{r}_n) = g(\mathbf{r}_n, \mathbf{r}_m)$ we introduce a symmetric matrix $\mathbf{G}$ where $G_{i,j} = g(\mathbf{r}_i, \mathbf{r}_j; k)$, the diagonal matrix $\hat{\mu}$ containing the coefficients μ_m and the vectors $\mathbf{A} = (A_0, \ldots, A_{N-1})^T$ and $\mathbf{U} = (u_i(\mathbf{r}_0), \ldots, u_i(\mathbf{r}_{N-1}))^T$. Writing the linear system of (8) as

$$(\mathbf{I} - \hat{\mu}\mathbf{G})\, \mathbf{A} = \hat{\mu}\mathbf{U} \tag{9}$$

allows for the amplitudes of the Green's functions to be solved for numerically. The formulation above, with each point possibly having its own mass and damping, is general; hereafter we simply take each point to be identically mass-loaded and undamped, unless explicitly stated otherwise.

3. Line Arrays and Rayleigh-Bloch Modes

As also noted in [23] it is possible, instead of applying forcing or an incident field, to look for localised states as solutions and in particular to consider an infinite periodic line array with each mass-loading separated by a characteristic length a, such that $\mathbf{r}_n = (na, 0)$ for $n \in \mathbb{Z}$. The periodicity of the geometry is exploited through the introduction of a Bloch wavenumber βa such that there is a phase-shift along the array of $A_n = e^{i\beta a} A_{n-1}$, making $A_n = e^{i\beta a n} A_0$ and $A_0 = \mu u(\mathbf{r}_0)$. A dispersion relation relating this phase-shift to wavenumber emerges from equation (7) when one considers the point $\mathbf{r}_0$

$$\frac{i(ka)^2}{2} \tilde{\mu} \sum_{n=-\infty}^{\infty} e^{i\beta a n} \left\{ H_0(ka|n|) - H_0(ika|n|) \right\} = 1 \tag{10}$$

where we discard the damping at each point $\tilde{\nu}_n$. This dispersion relation has a single real solution ka corresponding to each βa value $\beta a \in (0, \pi]$ where $\beta > k$

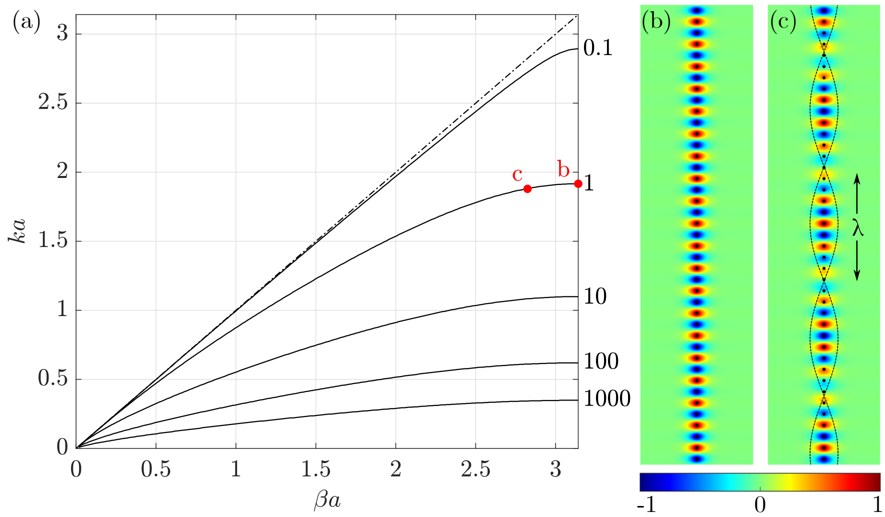

Figure 3: (a) Rayleigh-Bloch dispersion bands for an infinite line array of mass-loadings of uniform spacing, mass parameterised with increasing $\tilde{\mu}$ labelled on the right, calculated via eq. (6.3) of [23]. (b), (c) Real displacement fields for the corresponding points marked in (a). At the band edge (b), a standing waveform exists, characterised by a uniform long-scale amplitude. For frequencies away from the band edge, e.g. (c), a long scale envelope modulates the oscillations, resembling a beat frequency. The envelope wavelength, λ, is calculated using High Frequency Homogenisation (HFH) [27, 28] (Appendix A).

for finite $\tilde{\mu}$; infinite $\tilde{\mu}$ corresponds to pinned points and no solution exists in this case. The real solutions to (10), given in [23], correspond to Rayleigh-Bloch (RB) modes that propagate along the array and exponentially decay with distance perpendicular to the array. In Fig. 3(a) the dispersion bands describing Rayleigh-Bloch modes upon periodic line arrays are shown for several mass-loading parameters $\tilde{\mu}$, where the pinned limit is approached as $\tilde{\mu} \to \infty$. Figures 3(b) and (c) show the wavefields corresponding to the labels b and c along the $\tilde{\mu} = 1$ dispersion band in Fig. 3(a). The band flattens on approach to the band edge, resulting in a group velocity of zero and a standing wave solution in Fig. 3(b) with a modulating antisymmetric displacement existing only on a short-scale from point-to-point. Reducing the wavenumber from the band edge, to c, reveals an additional scale of wave propagation along the line array as in Fig. 3(c); the short-scale oscillations, as in Fig. 3(b), remain, but now are augmented by a long-scale beat envelope of characteristic wavelength, λ, defined by Eq. (11) of [28]. The long-scale is analyzed using the high-frequency-homogenization (HFH) method [28, 27, 29], with the envelope characterisation being useful in the identification of topological edge states [28] and the redirection of modes in multidirectional energy splitters [30]. In Sect. 4 analogous beat envelopes arise in the waveforms of whispering-Bloch modes, and their discrete wavenumbers correspond to an integer number of long-scale beat wavelengths circumnavigating the ring.

The relation (10) corresponds to an infinite line array along which Rayleigh-Bloch modes propagate. For the coupled ring-array system of Fig. 2, we have to either mimic the infinite line array, using an asymptotic approach [31], or truncate the infinite summation and solve a linear system of type (9) numerically. In the latter case, the truncation creates a spurious reflection of wave energy from the extremal points of the array. We remove these spurious reflections using an absorption layer of inclusions inserted into the linear system (9) for the vector of coefficients $\mathbf{A}$. We introduce point-wise damping $\tilde{\nu}_n$ for inclusions at the extremities of the truncated array in the parameter matrix $\hat{\mu}$.

A line array of forcings placed at $\mathbf{r}_n = (na, 0)$, for $n = 0 \ldots N-1$, have the left- and right-most N_d inclusions characterised by an impedance coefficient composed of an identical mass term $\tilde{\mu}$, but with an additional damping term $\tilde{\nu}(n)$ now a function of the summation index n, such that

$$\mu_d(n) = 4k^4 a^2 \tilde{\mu} + i4k^2 \tilde{\nu}(n). \tag{11}$$

The dependence of the damping term on position is taken as

$$\tilde{\nu}(n) = \frac{|N_d - n|^p}{N_d^p} \tilde{\nu}_0 \tag{12}$$

where p determines the rapidity, or rather smoothness, of the damping out of reflected modal energy, and $\tilde{\nu}_0$ is an arbitrary damping constant; such index-dependent damping is using for guided elastic waves in [32]. The vector of coefficients $\mathbf{A}$ is found through (9) using the parameter matrix

$$\hat{\mu} = \mathrm{diag}(\mu_d(1), \ldots, \mu_d(N_d), \mu, \ldots \mu, \mu_d(N_d), \ldots, \mu_d(1)) \tag{13}$$

where μ denotes identically all point-wise impedances in the undamped region of the truncated array. Equation (9) is augmented by the incident field for which we use excitation at the point $\mathbf{r}_f = (N_d + 1, 0)$ due to a forcing

$$u_i(\mathbf{r}) = g(\mathbf{r}, \mathbf{r}_f; k); \tag{14}$$

the wavenumber k corresponds to a Rayleigh-Bloch solution (10). As a validation, solving the new linearised system describing the truncated line array in isolation, the resulting wavefield in the fundamental unit cell matches identically that calculated via the theoretical Bloch wavenumber solution (6.5) of [23]. This method of absorption is implemented into all following line array-ring couplings and platonic circuits featured in Sect. 5, and makes possible the accurate determination of transmission coefficients in the through- and drop-ports of the proposed platonic filters.

4. Structured Ring Resonators and Whispering-Bloch Modes

4.1. Formulation for Point-Forcings

We consider structured ring resonators, and their resonant behaviours, for which we expect to encounter quasi-modes [33] i.e. complex solutions to a dispersion relation that are interpreted by analogy with the Rayleigh-Bloch modes upon line arrays. We consider the open system of a finite number of masses N placed, equally spaced, around the circumference of a circle with radius r_0. From (7), (8), in the absence of an incident field, the wavefield and amplitudes are

$$u(\mathbf{r}) = \sum_{n=0}^{N-1} A_n g(\mathbf{r}, \mathbf{r}_n; k), \qquad A_m = \mu \sum_{n=0}^{N-1} A_n g(\mathbf{r}_m, \mathbf{r}_n; k). \tag{15}$$

Bloch's theorem for a circular geometry follows by introducing $\hat{R}$, the discrete rotation operator of angle $2\pi/N$, for any function $f(r,\theta)$, by $\hat{R}f(r,\theta) = f(r, \theta + 2\pi/N)$. From rotational symmetry $u(\mathbf{r}) = u(r,\theta)$, and $\hat{R}u(r,\theta)$ satisfies the same eigenvalue problem as $u(r,\theta)$, and is equal up to a multiplicative constant σ such that $\hat{R}u(r,\theta) = \sigma u(r,\theta)$. Since $\hat{R}^N$ is the identity operator, we must have $\sigma^N = 1$ with σ being one of the N-th roots of unity, $\sigma = e^{2\pi i m/N}$ with $m \in \{0, \dots, N-1\}$.

In particular the amplitudes $A_n = A\left(a, 2n\pi/N\right)$ with $n \in \{0, \dots, N-1\}$. Applying this result, in the case where N is even, there exist $m \in \{0, .., N/2\}$ such that

$$A_n = e^{\pm 2\pi i n m/N} A_0 \tag{16}$$

where A_0 is an arbitrary constant; the positive and negative signs in the exponential lead to clockwise and anticlockwise spiralling solutions later, and we use the positive solutions hereafter. For a mode $m \in \{0, .., N/2\}$ the dispersion relation $\mathcal{D}(k,m) = 0$ is given by (15), when considering the point $\mathbf{r}_0$, leading to

$$\mathcal{D}(k,m) = \mu \sum_{n=0}^{N-1} e^{2\pi i n m/N} g(\mathbf{r}_0, \mathbf{r}_n; k) - 1 \tag{17}$$

and we solve for k as a given quasi-mode indexed by $m \in \{0, .., N/2\}$. We only consider solutions k such that

$$\mathrm{Real}(k) > 0 \quad \text{and} \quad \mathrm{Imag}(k) < 0. \tag{18}$$

These two conditions account for quasi-modes describing outward going solutions with vanishing energy at infinity i.e. $|\mathbf{r}| \to +\infty$.

In Fig. 4 we show a typical contour plot of $\log(|\mathcal{D}(k,m)|)$, for $N = 60$, $\tilde{\mu} = 1$ and $m = N/2 = 30$, that shows the existence of complex roots that are very close to the real axis. In Fig. 4 the solutions to the dispersion relation (17) are located at the sharp peaks for which $\log(|\mathcal{D}(k,m)|) \to -\infty$. The complex roots of the dispersion relation are found numerically using the winding number to

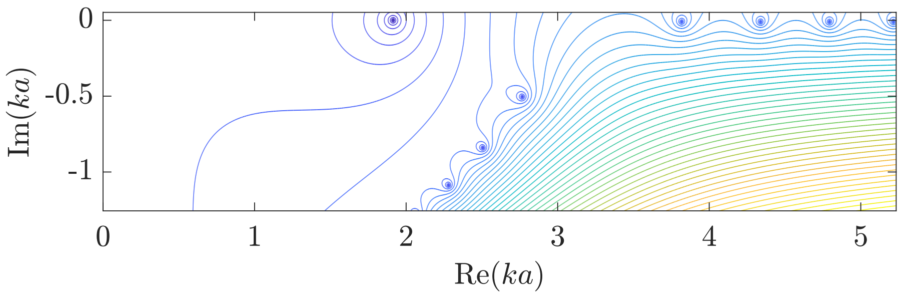

Figure 4: The behaviour of the dispersion relation in complex k space using $\log(|\mathcal{D}(k,m)|)$ shown as a contour plot for $N = 60$, $\tilde{\mu} = 1$ and $m = N/2 = 30$. Three types of solutions are immediately apparent; the isolated root of lowest $\mathrm{Re}(k)$ and $\mathrm{Im}(k)$ to the top left, the set of increasing $\mathrm{Re}(k)$ roots to the top right, and the set of increasing $\mathrm{Im}(k)$ roots centre-left. These solutions correspond to, respectively, the structure located, interior and decaying modes of the platonic ring resonator.

identify regions that contain a zero and the moments of the winding number to obtain its position [24, 34, 35]; given the high accuracy required to resolve the imaginary component these zeros were then refined using the built-in `fsolve` in `Matlab` that uses a Levenberg-Marquardt algorithm.

Figure 4 illustrates the non-uniqueness of solutions to (17) and several modes, for $m = 30$, occurring at different wavenumbers. Modes with a wavenumber close to $\mathrm{Im}(k) = 0$ are localised to the ring, whereas those of larger $\mathrm{Im}(k)$ decay too rapidly into the infinite plate to be retained by the structure. From the analysis of whispering-Bloch modes in [18, 24] we anticipate two families of modes belonging to a platonic ring resonator: structure-located whispering-Bloch (WB) modes and interior modes. Structure-located modes, that have the smallest value of $\mathrm{Re}(k)$ and $\mathrm{Im}(k)$ for any given m, are characterised by an antisymmetric field pattern localised to the inclusions defining the ring. The period of antisymmetry is defined by the given mode number m, and in the case of $m = N/2$ equals the arc-spacing between points - see Fig. 5(a) and (b). The antisymmetric structured mode $m = N/2$ has special significance, being analogous to the standing wave solution of Rayleigh-Bloch modes along the line array of Fig. 3(b) and being the most highly confined mode available to the ring.

The other family of modes, the interior modes, are localised to the cavity of the ring - see Fig. 5(c) and (d) - and correspond to solutions of greater $\mathrm{Re}(k)$ and $\mathrm{Im}(k)$ components along the top-right of Fig. 4. These solutions are characterised by the same antisymmetry of their line array structured counterparts, with an equal periodicity and a modulating field pattern now localised within the ring structure. In the small m case, these interior patterns begin to resemble whispering gallery modes observed in optical micro-disks [36] or on the interior of rings of infinitely long dielectric rods [37].

A key characteristic of both structured and interior solutions is the leakage

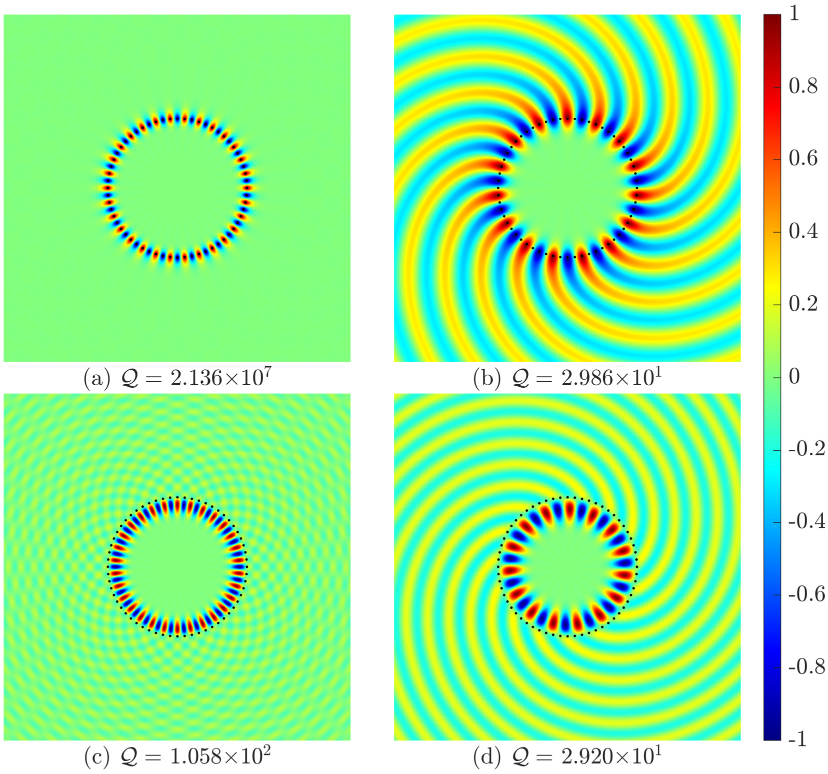

Figure 5: Real displacement fields for (a) the structure-located mode at modal value $m = N/2$, (b) the structure-located mode at modal value $m = N/4$, (c) the first interior mode at modal value $m = N/2$ and (d) the first interior mode at modal value $m = N/4$. Ring structure illustrated by black points.

of energy into the far-field, resulting in radiating Archimedean Spirals [38], as visible in Fig. 5(b) and (d). These radiation patterns appear as the wavenumber migrates from that of the antisymmetric $m = N/2$ solution, which itself defines the maximally structure-localised solution of minimal $\mathrm{Im}(k)$ component and hence minimal leakage. The spiralling patterns grow increasingly significant in the wavefields of resonance with growing $\mathrm{Im}(k)$ component as the selected mode decreases, visibly dominating the field pattern as in Fig. 8(b). These clockwise modes were selected by taking the positive sign of the exponent in (16), and identically reversed solutions exist for the negative sign. These radiation patterns are also visible in ring resonators composed of Neumann-type inclusions [38] and in the context of photonic crystal fibers [37, 39], featuring similar spirals in 'nearly bound states'. Hammer *et al.* provide the mode profiles of propagating TE modes as a function of bend radius of the waveguide [40], and in the following section we make similar considerations in our investigation of curvature-induced radiative losses.

4.2. Curvature-Induced Radiation Loss

The degree to which a quasi-mode of complex frequency is confined to a ring, or decays into the plate, is described quantitatively by the quality-factor, Q, of a WB mode. We define Q as

$$Q \stackrel{\text{def}}{=} \frac{\text{maximum energy stored in cycle}}{\text{energy lost per radian of cycle}} \sim \frac{\text{Re}(\omega)}{|2\text{Im}(\omega)|}, \tag{19}$$

where the expressions on the left- and right-hand-sides coincide in the limit $\text{Im}(\omega)/\text{Re}(\omega) \to 0$ [41]. Herein we calculate the limiting quality-factor in terms of complex wavenumber components as

$$\mathcal{Q} \stackrel{\text{def}}{=} \frac{\text{Re}(k^2)}{|2\text{Im}(k^2)|}, \tag{20}$$

for the quasi-mode solutions of (17) determined using the winding number method of [24]. As observed in rings consisting of Neumann inclusions embedded in thin-elastic plates [38, 41], the curvature-induced radiation loss experienced by a WB mode of given m rapidly falls as the number of points comprising the ring is increased; Fig. 6 shows the dependence of $\mathcal{Q}$ on N plotted on a logarithmic scale for three mode numbers. It is convenient to introduce an alternative definition of the mode number as

$$\Delta m = N/2 - m, \tag{21}$$

describing the 'modal distance' from the WB mode of greatest confinement, $m = N/2$. The $\text{Im}(k)$ component is observed to be exponentially small in angular period (see $\epsilon = \pi/N \to 0$ discussion in [41]) as the quasi-mode wavenumber migrates towards the real-axis to a corresponding RB wavenumber, and accordingly $\mathcal{Q}$ grows exponentially large in the same limit. The decline in $\mathcal{Q}$ with increasing modal distance corroborates the observed radiation leakage experienced by propagating WB modes; at $N = 60$ specifically, the contrasting spiralling patterns of radiation and lack thereof in Fig. 5(a) and (b) respectively illustrate the same decline in $\mathcal{Q}$ with Δm. In Tab. 1 we give values of the resonant wavenumbers k for different N corresponding to the structure-located and the first interior modes for which $m = N/2$ and $\tilde{\mu} = 1$.

Intuitively, the physical mechanism behind the leakage can be thought of in terms of direction of the propagating WB mode from point-to-point. Unlike the ring resonators of optical and photonic systems [36, 42], elastic ring resonators are characterised by their inclusion geometry of point- or Neumann-type inclusions equally spaced along the circumference of a circle, rather than through an effective refractive index and bend radius of a continuous waveguide. Introducing a curvature on the small-scale Bloch-periodic geometry causes a bending of the WB mode as it propagates from point-to-point, and this bending allows for the escape of flexural wave energy into the infinite plate. This is in contrast to

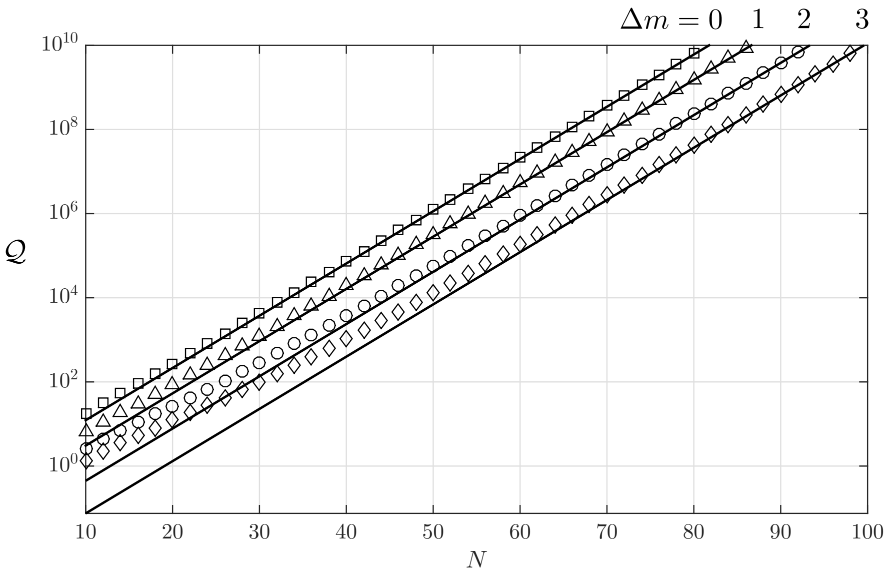

Figure 6: $\mathcal{Q}$ dependence belonging to rings of N point-masses of uniform mass-loading $\tilde{\mu} = 1$. Symbols are from calculation via dispersion relation (17), with different symbols used for different values of Δm. Solid lines are from asymptotic formula (6.24) of [41], formulated under considerations of the outer solution region. Figure adapted from [41].

N	Structure k	$\mathcal{Q}$	Interior k	$\mathcal{Q}$
20	$6.058 - 5.6 \times 10^{-3} i$	2.728×10^{2}	$14.825 - 9.4 \times 10^{-2} i$	3.935×10^{1}
40	$12.182 - 4.2 \times 10^{-5} i$	7.312×10^{4}	$25.791 - 9.2 \times 10^{-2} i$	6.987×10^{1}
60	$18.289 - 2.1 \times 10^{-7} i$	2.136×10^{7}	$36.480 - 8.7 \times 10^{-2} i$	1.054×10^{2}
80	$24.393 - 9.6 \times 10^{-10} i$	6.326×10^{9}	$47.035 - 8.2 \times 10^{-2} i$	1.442×10^{2}

Table 1: Table of complex wavenumbers for the structure-located and first interior modes for $m = N/2$ with corresponding limiting quality-factors $\mathcal{Q}$. Note the exponential growth in $\mathcal{Q}$ as $\pi/N \to 0$.

the line array, for which propagation of the field perpendicular to the guide is exponentially small with distance. In the limit of zero curvature $N \to \infty$, one expects a return to the RB case of no radiative losses and perfect localisation of the waveform to the structure. However, as the ring is both a finite and open system, one should always expect some leakage of energy into the plate for point-masses. Exponentially localised waveforms have been found by Movchan *et al.* [43] in rings devised of a finite number of mass-spring resonators for which the total mass and stiffness of the structure are set to result in a 'negative inertia', with real k identified via a homogenization model.

Mode localisation upon finite structures of resonators is desirable for the purposes of guiding and filtering flexural vibrations to a high-degree of precision and control. In Sect. 5 we analyze more geometrically complex elastic circuits of point-masses and the resonant behaviours that lie therein. For the purposes of ease of calculation and demonstration, we have selected rings of $N = 60$ point-masses of $\tilde{\mu} = 1$ and select only the highest $\mathcal{Q}$ modes available to minimise leakage into the plate. We demonstrate the guiding and filtering of flexural waves through ring resonator circuits and measure the resonant phenomena of the composite systems devised.

5. Ring-Array Coupling

5.1. Matching Solutions

The existence of Rayleigh- and whispering-Bloch modes upon similarly structured gratings suggests that a coupling between line arrays and ring resonators is feasible for the purposes of directing and manipulating wave motion in elastic plates. The analogy between such modes is made obvious by comparing the structure-located WB modes of lowest $\mathrm{Re}(k)$ for a ring resonator of N inclusions at modal values $m \in \{1, \ldots, N/2\}$ to the Rayleigh-Bloch dispersion band of Fig. 3(a) at $\tilde{\mu} = 1$. Scaling the spacing along the line array, a, to equal the linear distance between points along the ring, $a = 2\sin(\pi/N)$, the dispersion band for this ring-scaled array is superposed atop the discretised set of $\mathrm{Re}(k)$ WB solutions of the ring in Fig. 7(a). The antisymmetric mode of highest confinement $m = N/2$ corresponds to the standing wave solution $\beta = \pi/a$ located at the band edge, and modes of increasing Δm (and hence increasing leakage) migrate away from the band edge towards lower $\mathrm{Re}(k)$, reflecting the growing dominance of the $\mathrm{Im}(k)$ component and falling $\mathcal{Q}$.

The analogy between the guided Rayleigh-Bloch waves on the line array and the structured whispering-Bloch modes around the ring is further strengthened by inspecting the form of the wavefields in each regime. For a line array of point-masses there is a marked scale separation between the microstructure of the periodic cell and the macrostructure of the entire array; the supported Bloch waves are characterised by fast oscillatory solutions on the short scale modulated by an envelope function on the long scale, as shown in Fig. 3(c). The modulation, or beat wavelength of the RB wave is calculated using the High Frequency Homogenisation (HFH) asymptotic scheme [27], which leverages the multi-scale nature of the system by perturbing about the standing wave solutions present in the Bloch spectra at the edges of the Irreducible Brillouin Zone. This technique has recently been applied to line 1D arrays of point-masses on Kirchhoff-Love elastic plates [28], resulting in the governing equation (4) being reduced to an ODE entirely on the macroscale that incorporates the effects of the microstructure (see Appendix A). The array is then homogenised and the resulting ODE captures all the dispersive properties of the bands, described by the modulation of the strongly oscillating field. By considering a ring with the same inter-point spacings as the line array, this technique is used to estimate

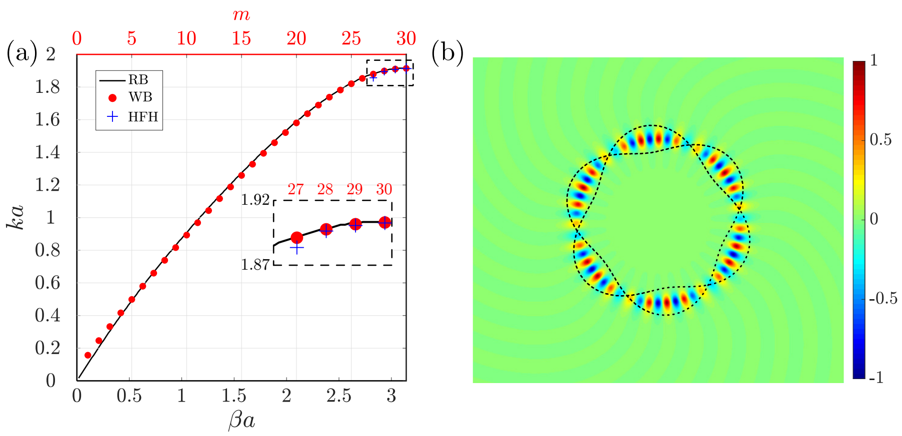

Figure 7: (a) The dispersion curve and discrete $\mathrm{Re}(k)$ solutions pertaining to a line array (solid line) and ring resonator (red points) at an impedance characterised by $\tilde{\mu} = 1$. Blue crosses correspond to predictions from the HFH calculations for which an integer number of wavelengths fit around the ring. The superposition of the RB curve atop the WB solutions and HFH approximations suggests a strong analogy between the guide and ring structure-located modes. (b) The real displacement wavefield pertaining to the $\Delta m = 3$ WB mode featuring three full beat wavelengths wrapped around the ring, illustrated by the superposed long-scale envelope.

several resonance modes of the ring in which integer numbers of the beat wavelength fit around the ring. These correspond to modes near the band edge of the line array as exemplified in Fig. 7(b).

The coupling geometry considered is based on that of Yariv [44] and is drawn schematically in Fig. 2(a); a line array of ring-scaled spacing is paired a distance d from a ring resonator of N point-masses. To ensure impedance matching (5) between line and ring, we assert the following condition on the impedance $\tilde{\mu}$

$$\tilde{\mu}_{line} a_{line}^2 = \tilde{\mu}_{ring} a_{ring}^2 \tag{22}$$

where a_{line} is the linear spacing along the line array and a_{ring} is the arc spacing along the ring, and these separations are equivalent in the limit $N \to \infty$. The relative angle between the nearest-neighbour points of the line array and ring is set to ensure minimal through-transmission along the guide downstream of the ring. The guide itself consists of $2M - 1$ points, for which an absorption layer of N_d inclusions is inserted on both ends obeying the damping profile (12). A Rayleigh-Bloch mode is triggered upon the guide via excitation at the point $\boldsymbol{r}_f = (N_d + 1, 0)$ such that the incident field is of the form (14). Given that RB modes are modes of real frequency, the frequency of excitation is selected such that it corresponds to the real part only of the lowest $\mathrm{Re}(k)$ solution to the dispersion relation (17) for any given m - the structure-located WB modes. Accordingly only these modes will be observed during coupling.

5.2. Measuring Transmission

The strength of coupling is described through the measurement of power radiated along the line array downstream of the ring. This is calculated using the following expression for the time-averaged flexural wave flux in a Kirchhoff-Love thin-elastic plate [45]

$$\langle \mathbf{F} \rangle = \frac{\Omega}{2} \mathrm{Im}\Big(u(\mathbf{r}) \nabla^3 u^*(\mathbf{r}) - \nabla^2 u^*(\mathbf{r}) \nabla u(\mathbf{r}) \Big), \tag{23}$$

where $u^*(\mathbf{r})$ denotes the complex conjugate of the displacement field (in fact, (23) is a 'simplified' flux. See [45]). This form of time-averaged flux is a statement of energy conservation in the plate: the surface integral of the time-averaged flux $\langle \mathbf{F} \rangle$ around any contour not enclosing a source must be zero. The power transmitted along the horizontal line array through a given unit cell ma is determined through integration of the quantity $\langle \mathbf{F} \rangle \cdot \hat{\mathbf{x}}$ along the boundaries of the corresponding infinite unit strip [46], such that

$$I = \int_{-\infty}^{\infty} \big(\langle \mathbf{F} \rangle \cdot \hat{\mathbf{x}} \big) \mathrm{d}y. \tag{24}$$

This integral of the time-averaged flux provides a measure of the wave energy propagating along the line array. We define the through-transmission coefficient T as the ratio of the radiated powers along the line in the presence of the ring and in isolation respectively - the latter being an unattenuated Rayleigh-Bloch solution - such that

$$T = \frac{I_T}{I_0}, \tag{25}$$

where both I_T and I_0 are measured at the boundary of the same unit strip downstream of the ring. The measurement of transmission over a narrow range of excitation frequencies provides an alternative definition of the quality-factor for a coupled ring-line array of real ω

$$Q_c \overset{\mathrm{def}}{=} \frac{\omega_r}{\Delta\omega}, \tag{26}$$

where Q_c is the quality-factor of coupling, ω_r is the resonant frequency in the measured transmission spectrum and $\Delta\omega$ is FWHM of the resonance peak. Using the definition $k^4 = m_p \omega^2 / D$, (26) is rewritten in terms of infinite plate wavenumber

$$Q_c = \frac{k_r^2}{\Delta(k^2)}, \tag{27}$$

where k_r is the wavenumber corresponding to the resonant frequency ω_r and $\Delta(k^2)$ is the FWHM of the resonant peaks in $1 - T$. Definition (27) should not be conflated with the limiting $\mathcal{Q}$ of the ring; the distinction being that $\mathcal{Q}$ quantifies the radiative losses suffered by ring-guided quasi-modes in isolation, whereas Q_c is a measure of the losses suffered by a ring-array coupler during coupling.

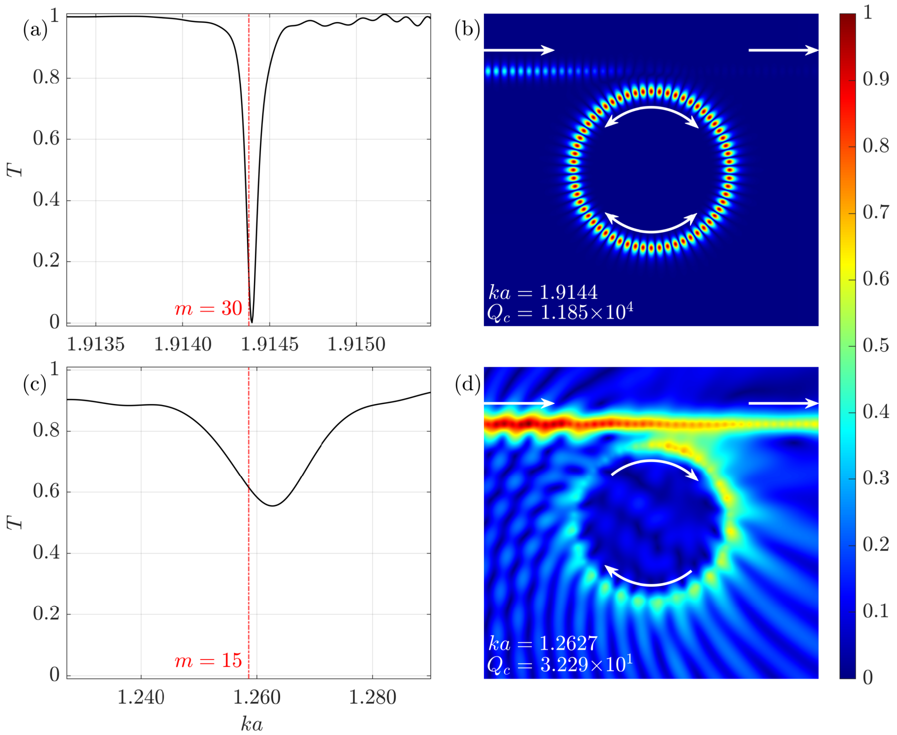

Figure 8: Transmission spectra about WB resonances for (a) $m = 30$ and (c) $m = 15$ for a ring of $N = 60$ mass-loadings, red dashed lines indicating WB resonances of (17). Minima in T corresponding to paired absolute displacement wavefields (b) and (d) for which $Q_c = 1.185 \times 10^4$ and $Q_c = 3.229 \times 10^1$ respectively.

Shown in Fig. 8 are the transmission spectra in the wavenumber regions about the WB (a) $m = N/2$ and (c) $m = N/4$ modes, WB wavenumbers labelled with vertical dashed lines. The resonances of the line-ring composite system are perturbed with respect to the WB resonances due to the presence of the neighbouring line array, with Fig. 8(a) $ka = 1.9144$ and (c) $ka = 1.2627$ corresponding to wavefields Fig. 8(b) and (d) respectively, and with Q_c values measured as (a) $Q_c = 1.185 \times 10^4$ and (b) $Q_c = 3.229 \times 10^1$. The wavefields Fig. 8(b) and (d) are plotted with absolute displacement values to highlight the attenuation of the propagating RB mode from the left-of-ring source, and the direction of the WB mode in propagation around the ring (ring geometry not shown hereafter for illustrative purposes). As is observed for conventional ring-guide couplers [15], a left-of-ring source produces a clockwise-propagating mode around the ring, with leakage arising due to the curvature of the circular array and spirals emanating from the structure in Fig. 8(d) as in Fig. 5(b). The coupling differs at the band edge wavenumber, at which the propagating RB mode acts as a standing wave source for flexural vibrations into the ring, and the propagation around the ring follows no preferential direction, as in Fig. 8(b). These mode trajectories can be observed in the time-averaged flux streamline plots of Appendix B calculated with (23).

We emphasise that the measure Q_c captures not the curvature induced losses experienced by the mode in propagation about the ring, but rather the radiative losses experienced during coupling. At wavenumbers at, or close to, the band edge the loss during coupling is at a minimum, and this is reflected by the sharp and narrow resonance peak of Fig. 8(a). The shallower and broader resonances characterising lower wavenumbers reflect weaker line-ring coupling and greater leakage into the plate, the latter being visible in the wavefield Fig. 8(c) as leakage emanating from the coupling region, and corroborated by the measure of Q_c being $\mathcal{O}(10^3)$ smaller at $m = 15$ than at $m = 30$. As energy leakage becomes increasingly characteristic of the coupling process with decreasing wavenumber, the measured Q_c falls towards zero, with the resonances in transmission growing increasingly shallow and broad and the filtering capabilities of the ring diminishing. This limit on the maximum Q_c available to the composite line-ring system has implications for the types of circuit geometries conceivable, and their ability to filter and direct flexural vibrations. In Sect. 5.3 we demonstrate the filtering of flexural waves in circuits of conjoined ring resonators, for which the highest Q_c modes were selected in order to minimise radiative losses during both propagation and coupling.

5.3. Coupled Resonator Elastic Arrays - CREAs

Like their optical counterparts (see CROWs [36, 47]), chains of coupled ring resonators in an elastic plate can be utilised as a means of directing and channeling vibrational energy: coupled resonator elastic arrays (CREAs) for the control of flexural wave motion. To this end, the first geometry we consider is the add-drop filter (ADF) of Fig. 2(b). The narrow-band nature, and depth of the transmission minima, at high m number - visible in Fig. 8(a) - suggests that line-ring coupling could be utilised for the purposes of narrow-band wave filtering. The upper line array defines the input- and through-ports and the lower the add- and drop-ports. The measure of drop-transmission coefficient is akin to that of the through-transmission coefficient

$$T = \frac{I_T}{I_0},\ D = \frac{I_D}{I_0}, \tag{28}$$

where I_T and I_D are the radiated powers measured downstream/upstream along the through- and drop-ports of Fig. 2(b) respectively, and I_0 the reference RB power in the absence of the ring.

For strong coupling and optimal wave filtering, hereafter we select only those modes at or near the band edge such that the radiative losses in propagation and the measured through-transmission coefficients are minimised. Shown in Fig. 9 are the displacement fields and T and D spectra near three WB resonances: (a) T and D spectra featuring peaks/dips near the WB (b) $m = 26$, (c) $m = 27$ and (d) $m = 28$ modes. The behaviours exhibited by the filter are similar to those

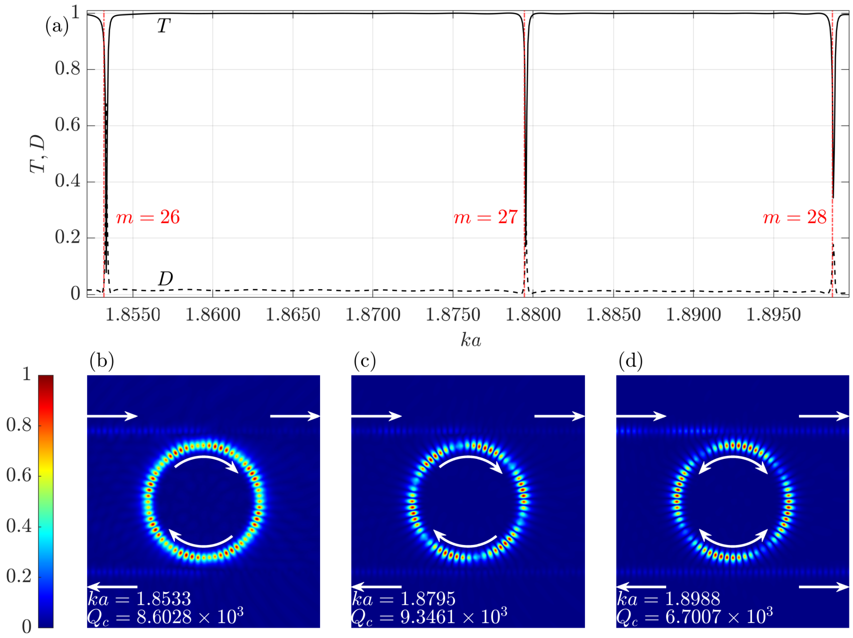

Figure 9: (a) T and D spectra in the wavenumber region of WB resonances (b) $m = 26$, (c) $m = 27$ and (d) $m = 28$, wavefields of absolute displacement. White arrows indicating directions of RB and WB propagation in line array and ring. Note that the highest WB modes feature bidirectional propagation in ring and array, (d), whereas lower resonances feature unidirectional propagation, (b) and (c).

exhibited by equivalent optical and photonic crystal ADFs [42, 48]; the transmission spectra Fig. 9(a) feature sharp peaks/dips in T and D close to the WB resonances, and the directionality of the WB mode is shown to be dependent on the wavenumber of excitation. Visible in the absolute displacement fields Fig. 9(b)-(d) is the attenuation of Through-port RB propagation, WB propagation around the ring, and the transmission of an RB mode unidirectionally or bidirectionally along the output array. The bidirectional or unidirectional RB propagation in the output array is dependent on the selected resonance, with bidirectional propagation observed at resonances closest to the band edge and unidirectional propagation occurring at resonances at or below the $m = 27$ resonance. Like the coupling of Fig. 8(b), at band edge adjacent wavenumbers the RB mode acts as a standing wave source of flexural vibrations into the ring with no preferential direction; both clockwise and anticlockwise WB circulation results in transmission into both the drop- and add-ports of the output array, as in Fig. 9(d). In Fig. 9(b) and (c) the ring-guided mode is purely clockwise with transmission predominantly into the drop-port, and both fields feature stronger attenuation of RB propagation along the input array, corroborating the sharper dips in through-transmission in Fig. 9(a) measured at these resonances. See Appendix B for the flux streamline plots illustrating the described mode directionality.

At these band edge adjacent wavenumbers Fig. 9(b)-(d), analogous long-scale envelopes to those along the linear array calculated via HFH (Fig. 7(a)) are observed along the ring during coupling, with integer number of beat wavelengths circumnavigating the ring in each case. As in Fig. 8(b), the Q_c (measured with the peaks in $1 - T$) are of the order $Q_c = \mathcal{O}(10^3) - \mathcal{O}(10^4)$ and decline with distance from the band edge, reflecting the increase in energy loss during coupling. We note that the highest quality-factor of coupling available to the composite system belongs to the first resonance featuring purely unidirectional motion, in this case the resonance near the $m = 27$ WB mode, and that this is a consequence of the measurement of T (and hence Q_c) being downstream of the ring.

Next we consider CREAs consisting of multiple rings chained horizontally, such that neighbouring rings couple with one-another and the leading and trailing rings couple with the bordering line arrays. By introducing additional rings we expect to observe resonant behaviours that differ from those of the isolated ring or single-ring ADF, including multiple resonances in transmission about each WB resonance [49] and alternating waveforms from ring-to-ring, visible in the field pattern at each resonance [36, 42]. Referred to as 'supermodes' in [36, 42], a given WB resonance of the isolated ring splits into a series of peaks/dips about the central WB wavenumber. As stated in [42], a Fourier harmonic system is revealed in the field patterns of the resonances; rings in 'off-states' being nodes and neighbouring 'on-state' rings antinodes, with the supermode resonances defining the set of observable harmonics and the fundamental harmonic being that of the lowest frequency. The number of rings also determines the direction of add- and drop-ports in the output guide, with an even number of rings reversing the drop-port direction relative to the ADF and an odd number retaining it. The propagation remains bidirectional at band edge adjacent wavenumbers, as in Figs. 8(b) and 9(d).

Shown in Figs. 10 and 11 are the transmission spectra and corresponding resonant wavefields for the CREAs consisting of two and three rings respectively, in the wavenumber region about the WB $m = 27$ wavenumber. This mode was chosen as it corresponds to the highest coupling quality-factor available to the ADF - see Fig. 9(b) - for which the output mode propagation was observed to be primarily through the drop-port. In Fig. 10, the T and D spectra pertaining to a two-ring system have split into a series of multiple resonances about the central WB wavenumber; four narrow-band resonances are measured, of Q_c values of the order $Q_c = \mathcal{O}(10^4)$, with all resonances corresponding to bidirectional propagation through the CREA system. The absolute displacement wavefields Fig. 10(b) and (c) correspond to the left-of-centre resonances from left to right, with each exhibiting a mirror symmetry about the mid-point between the rings. The ring-guided modes feature the long-scale beat-waveform of Fig. 7(b), where the waveforms of Fig. 10(c) are a rotation of those of Fig. 10(b) through half

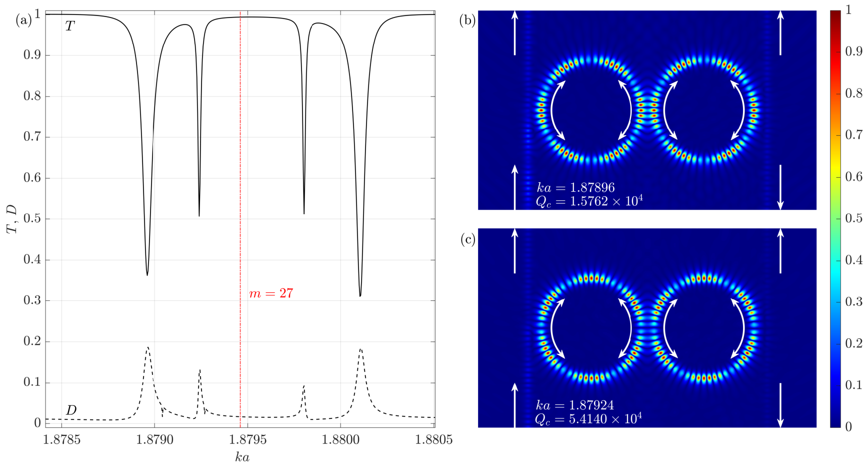

Figure 10: (a) Transmission spectrum about the WB $m = 27$ wavenumber for a two-ring CREA, where the left-of-centre resonances correspond to absolute wavefields (b) and (c) from left to right. The mode propagation being bidirectional throughout the CREA system at all resonances.

a beat wavelength. Consequently as the stronger outer resonances are characterised by waveforms of an antinode at the line-ring interface, the weaker inner resonances are characterised by a node at the line-ring interface. This observation corroborates the shallower measured dips or peaks in T or D, with an antinode associated with maximal input attenuation and drop-transmission, and a node minimal input attenuation and drop-transmission. The shape of the waveforms are repeated about the central wavenumber, such that the resonances to the right of the central wavenumber are reflections of those on the left about the centroid of each ring (for more detail, see Fig. 12).

To emphasise the symmetries available to the CREAs we include a second example with an odd number of rings. In Fig. 11 the transmission spectra for a CREA of three rings has split into a set of five resonances over the same wavenumber region about the central WB $m = 27$ wavenumber, of Q_c values again of order $Q_c = \mathcal{O}(10^4)$. The absolute displacement wavefields Fig. 11(b)-(d) correspond to the left-of-centre resonances of Fig. 11(a) from left to right, and each features a mirror symmetry now about the centroid of the central ring in the chain. The circulating ring modes include the long-scale beat-waveform of the $m = 27$ WB mode, and the inner resonance waveforms are again rotations of the outer resonance waveforms through half a beat wavelength. As for the two-ring CREA the weaker resonances are associated with a node at the line-ring interface and the stronger resonances an antinode, with all four outer resonances corresponding to bidirectional motion throughout the CREA. The strong central peak/dip in transmission is a mode of purely unidirectional motion through the CREA (see Fig. 11(d)), akin to the alternating clockwise-anticlockwise ring

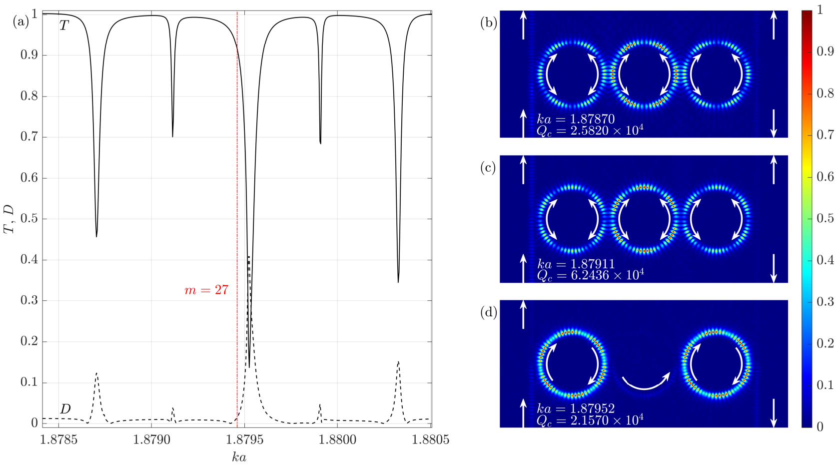

Figure 11: (a) Transmission spectrum about the WB $m = 27$ wavenumber for a three-ring CREA, where the left-of-centre resonances correspond to absolute wavefields (b), (c) and (d) from left to right. Mode propagation being (b) bidirectional, (c) bidirectional and (d) unidirectional throughout the CREA system. Note the central ring of (d), with propagation exclusively along the lower arc, being in an 'off-state'.

networks of Hammer *et al.* [42, 36] or Poon *et al.* [50, 51]. This resonance occurs at the same wavenumber as that measured near the WB $m = 27$ resonance of the single ring ADF - see Fig. 9(c) for which $ka = 1.8795$ - and like the circulating waves of [51] Sect. 2B is interpreted as a superpositon of WB modes belonging to the ring resonators. The resulting output transmission is purely into the drop-port to the bottom right, with little leakage of energy into the add-port. See Appendix B for the flux streamlines denoting the directionality of these modes. The central resonance of Fig. 11(a) and lack thereof of Fig. 10(a) suggests that odd-numbered CREAs are better candidates for flexural wave filters, with the same shape in transmission spectra observed around other band edge adjacent modes for the two- and three-ring CREAs.

To emphasise the variety of available resonant states belonging to CREA systems, displayed in Fig. 12 are the collection of field patterns (a)-(i) belonging to a CREA of nine ring resonators around the $m = 30$ WB mode. The emergent pattern resembles closely that of Hammer [42] Fig. 5 ordered (a)-(i) belonging to a CROW of nine rings. Features include off-state and on-state rings and the strongest output transmission at the central resonance Fig. 12(e). The resonant waveforms each hold a mirror symmetry about the central ring, with the waveforms Fig. 12(f)-(i) being reflections of those (a)-(d) about the centroid of each ring. The circulation throughout the chain is bidirectional at all wavenumbers of resonance, each ka being adjacent to the band edge of Fig. 7(a) at which the standing wave source induces bidirectional coupling.

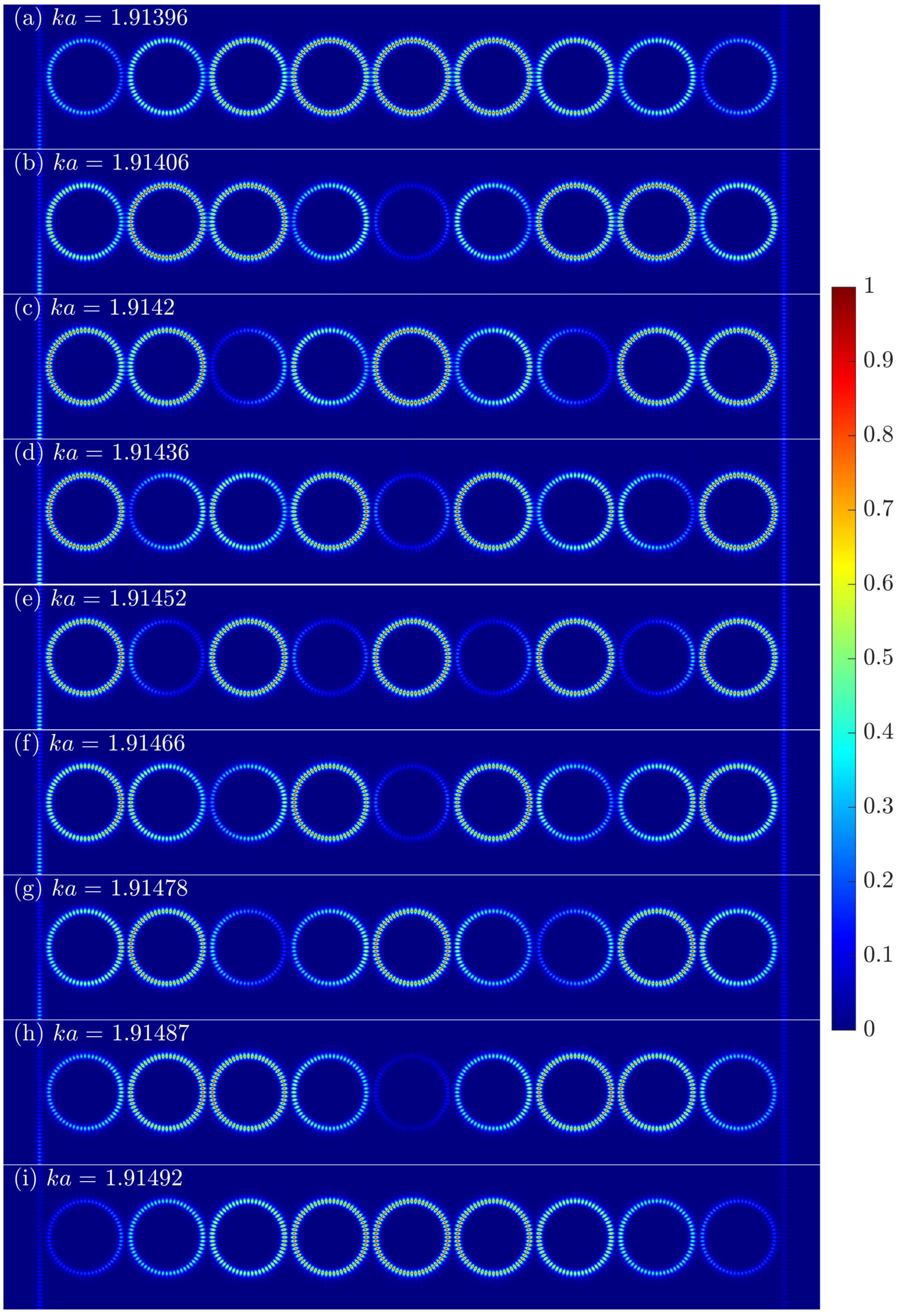

Figure 12: Absolute displacement field patterns at supermode resonances about the WB $m = 30$ resonance for a CREA system consisting of nine ring resonators. A similar set of harmonics are observed around all WB modes for the nine-ring CREA.

6. Concluding Remarks

Here we have demonstrated a high degree of control in the directing and filtering of flexural waves in thin-elastic plates governed by Kirchhoff-Love thin-plate theory. Arrays of mass-loadings of a high degree of rotational symmetry have been shown to support whispering-Bloch quasi-modes of complex wavenumber, analagous to the Rayleigh-Bloch modes upon infinite line arrays of [23]. These WB modes are characterised by a discrete set of solutions to the dispersion relation (17), with imaginary component quantifying the leakage of energy into the far-field. The non-uniqueness of solutions reveals two families of modes: structure-located WB modes and interior modes, the former being analagous to RB modes upon linear guides, the latter provided a detailed analysis in [24]. The achieved limiting quality-factor of the structure-located WB modes is of the order $\mathcal{Q} = \mathcal{O}(10^7)$ for a ring of $N = 60$ point-masses at $m = N/2$, and has been shown to grow exponentially large in the limit $N \to \infty$ [41]. The analogy between the RB and WB solutions is strengthened by the determination of the long-scale envelope wavelength via the HFH scheme of [28], demonstrating that the WB solutions adjacent to the band edge correspond to an integer number of wavelengths circumnavigating the ring. Line-ring coupling has allowed for the filtering of flexural waves incoming along the line array, with the measurement of radiated power providing an alternative definition of the quality-factor (27) for the line-ring composite systems, herein coined CREAs. The add-drop filter and CREAs of an even and odd number of rings have been conceptualised, with quality-factors of order $Q_c = \mathcal{O}(10^3) - \mathcal{O}(10^4)$, and exhibit both unidirectional and bidirectional mode propagation. The ADF in particular acts as an effective filter for RB output exclusively along the drop-port at those wavenumbers first exhibiting purely clockwise circulation. Similarly, the central resonance of the three-ring CREA corresponds to purely clockwise-anticlockwise circulation, for which the output is exclusively along the drop-port.

Herein we have presented an array of interesting flexural wave phenomena, and this work holds promising extensions to the design of platonic devices. One such example could be the grading of ring radii along the CREA as a means of rainbow trapping [28] for energy harvesting networks like those of [46, 52]. An analogous application in the realm of optics of equivalent CROWs is the slowing of transmission and group velocity of light for the purposes of engineering optical delay lines [50, 53]. In replicating this, exponentially localised waveforms are of particular importance, and in the realm of elasticity this could be achieved through the inclusion of mass-spring ring resonators of negative inertia and real k [43], deemed 'negative inertial circuits'.

Acknowledgments

H.J. Putley is grateful for EPSRC (UK) funding provided through the Centre for Doctoral Training "Fluid Dynamics Across Scales" Programme grant no. EP/L016230/1.

G.J. Chaplain gratefully acknowledges financial support from the EPSRC in the form of a Doctoral Prize Fellowship.

B. Maling gratefully acknowledges funding provided by EPSRC (UK) through Programme grant no. EP/L024926/1

References

[1] J.D. Kaplunov, L.Y. Kossovich, and E.V. Nolde. *Dynamics of Thin Walled Elastic Bodies*. Academic Press, New York, 1998.

[2] D.J. Mead. Wave propagation in continuous periodic structures: research contributions from Southampton 1964-1995. *J. Sound Vib.*, 190:495–524, 1996.

[3] B.R. Mace. The vibration of plates on two-dimensionally periodic point supports. *J. Sound Vib.*, 192:629–643, 1996.

[4] R.S. Langley. The response of two-dimensional periodic structures to point harmonic forcing. *J. Sound Vib.*, 197:447–469, 1997.

[5] A.B. Movchan, N.V. Movchan, and R.C. McPhedran. Bloch-Floquet bending waves in perforated thin plates. *Proceedings of the Royal Society A: Mathematical, Physical and Engineering Sciences*, 463:2505–2518, 2007.

[6] R.C. McPhedran, A.B. Movchan, and N.V. Movchan. Platonic crystals: Bloch bands, neutrality and defects. *Mech. Mater.*, 41:356–363, 2009.

[7] M. Farhat, S. Guenneau, S. Enoch, A.B. Movchan, and G. Petursson. Focussing bending waves via negative refraction in perforated thin plates. *Appl. Phys. Lett.*, 96:081909, 2010.

[8] M. Farhat, S. Guenneau, and S. Enoch. High directivity and confinement of flexural waves through ultra-refraction in thin perforated plates. *Euro. Phys. Lett.*, 91:54003, 2010.

[9] D. Torrent, D. Mayou, and J. Sanchez-Dehesa. Elastic analog of graphene: Dirac cones and edge states for flexural waves in thin plates. *Phys. Rev. B*, 87:115143, 2013.

[10] S.G. Haslinger, R.V. Craster, A.B. Movchan, N. V. Movchan, and I. S. Jones. Dynamic interfacial trapping of flexural waves in structured plates. *Proceedings of the Royal Society A: Mathematical, Physical and Engineering Sciences*, 472:20150658, 2016.

[11] R.V. Craster T. Antonakakis and S. Guenneau. Moulding and shielding flexural waves in elastic plates. *Euro. Phys. Lett.*, 105:54004, 2014.

[12] G.C. Righini, Y. Dumeige, P. Féron, M. Ferrari, G. Nunzi Conti, D. Ristic, and S. Soria. Whispering gallery mode microresonators: Fundamentals and applications. *Rivista Del Nuovo Cimento*, 34:435–488, 2011.

[13] F. Vollmer and S. Arnold. Whispering-gallery-mode biosensing: label-free detection down to single molecules. *Nature Methods*, 5:591–596, 2008.

[14] V.S. Ilchenko, A.A. Savchenko, Matsko A.B., and Maleki L. Nonlinear Optics and Crystalline Whispering Gallery Mode Cavities. *Phys. Rev. Lett.*, 92, 2004.

[15] D.G. Rabus. *Ring Resonators: Theory and Modeling*, pages 3–40. Springer Berlin Heidelberg, Berlin, Heidelberg, 2007.

[16] W. Bogaerts, P. De Heyn, T. Van Vaerenbergh, K. De Vos, S. Kumar Selvaraja, T. Claes, P. Dumon, P. Bienstman, D. Van Thourhout, and R. Baets. Silicon microring resonators. *Laser & Photonics Reviews*, 6(1):47–73, 2012.

[17] A.B. Matsko, A.A. Savchenkov, D. Strekalov, V.S. Ilchenko, and L. Maleki. Review of Applications of Whispering-Gallery Mode Resonators in Photonics and Nonlinear Optics. *IPN Progress Report*, 2005.

[18] B. Maling and R.V. Craster. Whispering Bloch modes. *Proceedings of the Royal Society A: Mathematical, Physical and Engineering Sciences*, 472:20160103, 2016.

[19] R. Porter and D.V. Evans. Rayleigh-Bloch surface waves along periodic gratings and their connection with trapped modes in waveguides. *J. Fluid Mech.*, 386:233–258, 1999.

[20] J.B. Pendry, L. Martín-Moreno, and F.J. Garcia-Vidal. Mimicking Surface Plasmons with Structured Surfaces. *Science*, 305, 2004.

[21] R.A. Hurd. The propagation of an electromagnetic wave along an infinite corrugated surface. *Can. J. Phys.*, 32:727–734, 1954.

[22] D. Sengupta. On the phase velocity of wave propagation along an infinite Yagi structure. *IRE Trans. Antennas Propag.*, 7:234–239, 1959.

[23] D.V. Evans and R. Porter. Penetration of flexural waves through a periodically constrained thin elastic plate in vacuo and floating on water. *Journal of Engineering Mathematics*, 58(1-4):317–337, 2007.

[24] H. Rakotoarimanga-Andrianjaka. Platonic whisperings: Coupling of elastic ring-resonators and waveguides. Master's thesis, Imperial College London, 2016.

[25] S.P. Timoshenko and S. Woinowsky-Krieger. *Theory of plates and shells.* McGraw-hill, 1959.

[26] L.R.F. Rose and C.H. Wang. Mindlin plate theory for damage detection: Source solutions. *The Journal of the Acoustical Society of America*, 116(1):154–171, 2004.

[27] R.V. Craster, J. Kaplunov, and A.V. Pichugin. High-frequency homogenization for periodic media. *Proceedings of the Royal Society A: Mathematical, Physical and Engineering Sciences*, 466(2120):2341–2362, 2010.

[28] G.J. Chaplain, M.P. Makwana, and R.V. Craster. Rayleigh–Bloch, topological edge and interface waves for structured elastic plates. *Wave Motion*, 86:162–174, 2019.

[29] T. Antonakakis and R.V. Craster. High frequency asymptotics for microstructured thin elastic plates and platonics. *Proceedings of the Royal Society A: Mathematical, Physical and Engineering Sciences*, 468:1408–1427, 2012.

[30] M.P. Makwana and R.V. Craster. Designing multidirectional energy splitters and topological valley supernetworks. *Phys. Rev. B*, 98(23):235125, 2018.

[31] G.M. Lynott, V. Andrew, I.D. Abrahams, M.J. Simon, W.J. Parnell, and R.C. Assier. Acoustic scattering from a one-dimensional array; Tail-end asymptotics for efficient evaluation of the quasi-periodic Green's function. *Wave Motion*, 89:232–244, 2019.

[32] E.A. Skelton, S.D.M. Adams, and R.V. Craster. Guided elastic waves and perfectly matched layers. *Wave Motion*, 44(7-8):573–592, 2007.

[33] E.S.C. Ching, P.T. Leung, A. Maassen van den Brink, W.M. Suen, S.S. Tong, and K. Young. Quasinormal-mode expansion for waves in open systems. *Rev. Mod. Phys.*, 1998.

[34] L.M. Delves and J.N. Lyness. A numerical method for locating the zeros of an analytic function. *Mathematics of Computation*, 21(100):543–560, 1967.

[35] P.R. Brazier-Smith and J.F.M. Scott. On the determination of the roots of dispersion equations by use of winding number integrals. *J. Sound Vib.*, 145(3):503–510, 1991.

[36] E.F. Franchimon, K.R. Hiremath, R. Stoffer, and M. Hammer. Interaction of whispering gallery modes in integrated optical microring or microdisk circuits:Hybrid Coupled Mode Theory model. *J. Opt. Soc. B*, 30(4):1048–1057, 2013.

[37] E.N. Bulgakov and A.F. Sadreev. Nearly bound states in the radiation continuum in a circular array of dielectric rods. *Phys. Rev. A*, 97(3):033834, 2018.

[38] B. Maling, O. Schnitzer, and R.V. Craster. Radiation from structured-ring resonators. *SIAM Journal on Applied Mathematics*, 77(3):1047–1067, 2017.

[39] E.N. Bulgakov and A.F. Sadreev. Fibers based on propagating bound states in the continuum. *Phys. Rev. B*, 98(8):085301, 2018.

[40] M. Hammer, K.R. Hiremath, and R. Stoffer. Analytical approaches to the description of optical microresonator devices. In *AIP Conference Proceedings*, volume 709, pages 48–71. American Institute of Physics, 2004.

[41] B. Maling. *Asymptotic analysis of array-guided waves.* PhD thesis, Imperial College London, 2016.

[42] M. Hammer. HCMT models of optical miroring-resonator circuits. *J. Opt. Soc. B*, 27:2237–2246, 2010.

[43] A.B. Movchan, R.C. McPhedran, G. Carta, and R.V. Craster. Platonic localisation: one ring to bind them. *Archive of Applied Mechanics*, 89(3):521–533, 2019.

[44] A. Yariv. Universal relations for coupling of optical power between microresonators and dielectric waveguides. *Electronics Letters*, 36(4):321–322, 2000.

[45] A.N. Norris and C. Vemula. Scattering of flexural waves on thin plates. *J. Sound Vib.*, 181(1):115–125, 1995.

[46] G.J. Chaplain, D. Pajer, J.M. De Ponti, and R.V. Craster. Delineating rainbow reflection and trapping with applications for energy harvesting. *New Journal of Physics*, 2020.

[47] A. Yariv, Y. Xu, R.K. Lee, and A. Scherer. Coupled-resonator optical waveguide: a proposal and analysis. *Optics Letters*, 24(11):711–713, 1999.

[48] S. Robinson and R. Nakkeeran. Photonic crystal ring resonator-based add drop filters: a review. *Optical Engineering*, 52(6):060901, 2013.

[49] F. Morichetti, A. Melloni, A. Breda, A. Canciamilla, C. Ferrari, and M. Martinelli. A reconfigurable architecture for continuously variable optical slow-wave delay lines. *Optics Express*, 15(25):17273–17282, 2007.

[50] J.K.S. Poon, J. Scheuer, S. Mookherjea, G.T. Paloczi, Y. Huang, and A. Yariv. Matrix analysis of microring coupled-resonator optical waveguides. *Optics Express*, 12(1):90–103, 2004.

[51] J.K.S. Poon, J. Scheuer, Y. Xu, and A. Yariv. Designing coupled-resonator optical waveguide delay lines. *J. Opt. Soc. B*, 21(9):1665–1673, 2004.

[52] J.M. De Ponti, A. Colombi, R. Ardito, F. Braghin, A. Corigliano, and R.V. Craster. Graded elastic metasurface for enhanced energy harvesting. *New Journal of Physics*, 22(1):013013, 2020.

[53] J.K.S. Poon, L. Zhu, G.A. DeRose, and A. Yariv. Transmission and group delay of microring coupled-resonator optical waveguides. *Optics Letters*, 31(4):456–458, 2006.

[54] M. Makwana, T. Antonakakis, B. Maling, S. Guenneau, and R.V. Craster. Wave mechanics in media pinned at Bravais lattice points. *SIAM Journal on Applied Mathematics*, 76(1):1–26, 2016.

Appendix A. High Frequency Homogenisation

Here we briefly outline the High Frequency Homogenisation scheme, which follows that in [28], used to approximate several WB ring resonance frequencies by inspecting the beat wavelength of a line array with the same inter-point spacing. High Frequency Homogenisation rests on separating the spatial coordinates into two scales to be treated independently. The periodic nature of the 1D array naturally characterises a short scale, defined by the coordinates $\boldsymbol{\xi} = (x/l, y/l)$, with l being commensurate with the periodicity. A long scale $X = x/L$ is then defined on the order of the length of the entire array, characterised by L. Assuming that $\epsilon \equiv l/L \ll 1$, we expand both the wavefield and frequency of the standing wave solutions (at the band edge) to derive an effective medium ordinary differential equation (ODE) for the long scale modulated by oscillatory behaviour on the short scale. The resulting equation describes the long-scale envelope function $f(X)$ through

$$f_{,XX} - \tilde{T} f = 0, \tag{A.1}$$

where $\tilde{T} = \left(\frac{k^4 - k_0^4}{T}\right)$: k_0 is the frequency at the band edge with k corresponding to the frequency of excitation, and T is a quantity that can be evaluated in several ways, depending on how the dispersion relations are obtained. In certain scenarios an exact analytical form relates T to integral quantities of the wavefield [54], whereas here we opt to obtain it from a Fourier-Hermite-Galerkin (FHG) method, specifically developed for calculating the dispersion curves for RB arrays in thin plates [28]. The sign of $\tilde{T}$ then determines the characteristic decay envelope (for $k > k_0$) or beat wavelength (for $k < k_0$). By calculating this wavelength we are able to estimate the frequencies supported along a line array

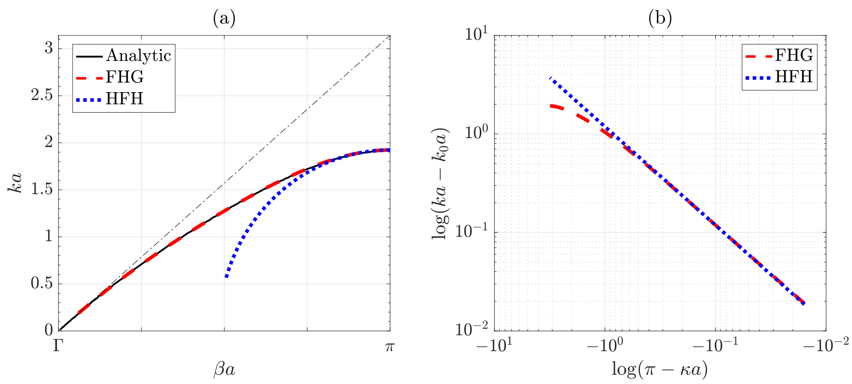

Figure A.13: (a) Dispersion curves for line RB array ($\tilde{\mu} = 1$) calculated analytically as in [23] (solid black), using the FHG scheme as in [28] (dashed red) with the corresponding HFH asymptotics (dotted blue). (b) Loglog plots confirming HFH accuracy.

that correspond to a WB resonance around a discrete ring array (assuming the same inter-point spacing), by matching an integer number of wavelengths of the beat wavelength around the ring - shown in Fig. 7. The dispersion curves calculated by the FHG method match those calculated as in [23], as shown in Fig. A.13, which additionally shows the asymptotic approximation of the dispersion relation obtained by the HFH scheme.

Appendix B. Time-Averaged Flux

The time-averaged flux equation, repeated here for convenience

$$\langle \mathbf{F} \rangle = \frac{\Omega}{2} \mathrm{Im}\Big(u(\mathbf{r}) \nabla^3 u^*(\mathbf{r}) - \nabla^2 u^*(\mathbf{r}) \nabla u(\mathbf{r}) \Big), \tag{B.1}$$

describes the flux at any point $\mathbf{r}$ in the x-y plane, averaged over one period. As explained in [45] $\mathbf{F}$ is a simplified flux that is 'more suitable for use in practice', and when time-averaged coincides with the time-average of the 'true' flux. This makes it an ideal quantity for the purposes of illustrating the average motion of flexural vibrations through the line-ring couplers of Sect. 5. The first of these we consider is the single line-ring coupler of Fig. 8(b) and (d), with emphasis on the coupling region between line and ring. In Fig. B.14 we superpose the time-averaged flux streamlines atop the normalised absolute displacement fields of Fig. 8(b) and (d). In Fig. B.14(a) the coupling into the ring is observably bidirectional; the group velocity of the incident Rayleigh-Bloch wave is close to zero, allowing for the incident RB mode to reverse direction during coupling and propagate anticlockwise around the ring. In Fig. B.14(b) the higher group velocity leads to exclusively clockwise propagation in the ring with no reversal, and this is the observed case in the field plots at resonances away from the band edge.

Next, the time-averaged flux through the output-port of the ADF is shown superposed atop the normalised absolute displacement fields of Fig. 9(b) and (c) in Fig. B.15. In Fig. B.15(a) at $m = 26$ the output is almost exclusively through the drop-port due to a clockwise propagating mode in the ring, with flux curves appearing within the add-port due to radiation leakage from the ring. In Fig. B.15(b) at $m = 27$ the clockwise ring mode couples into the output guide primarily through the drop-port to the left, although due to its proximity to the band edge exhibits some reversal into the add-port to the right.

To illustrate the bidirectional and unidirectional coupling through the larger CREA systems, we include the flux streamlines superposed atop the normalised displacement fields of the three-ring CREA of Fig. 11 at a bidirectional wavenumber Fig. B.16(a) and a unidirectional wavenumber Fig. B.16(b). Shown at the interface between the leading and central ring, the bidirectional mode of Fig. B.16(a) corresponds to that of Fig. 11(b) and the unidirectional mode Fig. B.16(b) to Fig. 11(d). Note the reversal of flux streamlines in B.16(a) highlighting the lack of preferential direction.

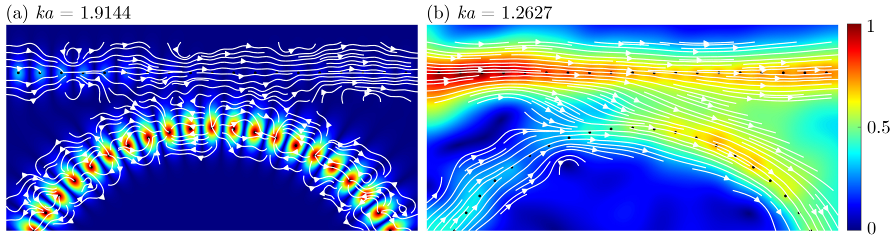

Figure B.14: Flux streamlines plotted atop absolute displacement fields at wavenumbers of resonance (a) $ka = 1.9144$ and (b) $ka = 1.2627$ for the line-ring coupler. Panel (a) demonstrates the lack of a preferential direction around the ring at the $m = 30$ resonance, whereas (b) demonstrates purely clockwise ring propagation. Geometry included for clarity.

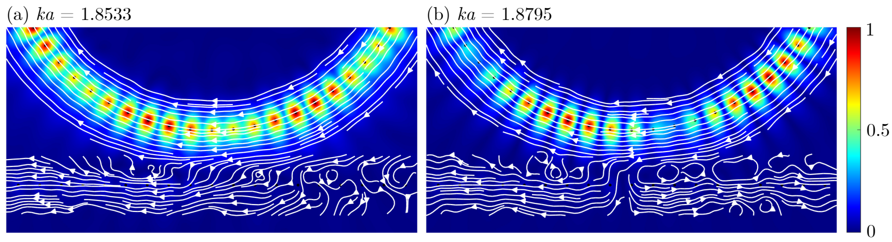

Figure B.15: Flux streamlines plotted atop absolute displacement fields at wavenumbers of resonance (a) $ka = 1.8533$ and (b) $ka = 1.8795$ for the ADF. Panel (a) displays transmission exclusively through the drop-port whereas (b) displays propagation primarily into the drop-port, with some reversal along the add-port due to the proximity of the $m = 27$ mode to the band edge.

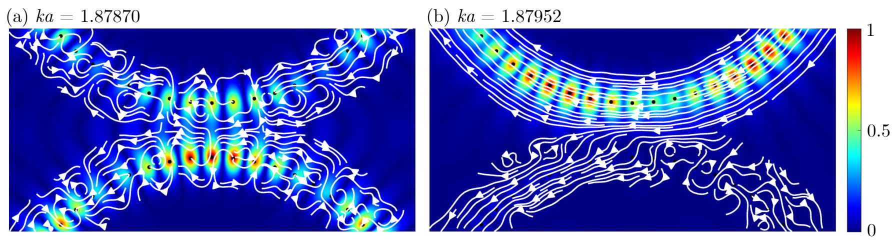

Figure B.16: Flux streamlines plotted atop absolute displacement fields at wavenumbers of resonance (a) $ka = 1.87870$ and (b) $ka = 1.87952$ at the first ring-ring interface of the three-ring CREA. Panel (a) displaying no preferential direction along either ring and (b) an anticlockwise circulation in the central ring due to a clockwise circulation in the leading ring. Wavefields rotated for consistency with Figs. B.14 and B.15.